RSC Advances

PAPER

View Article Online
View Journal | View Issue

Cite this: *RSC Adv.*, 2023, **13**, 25305

Catalytic evaluation and *in vitro* bacterial inactivation of graphitic carbon nitride/carbon sphere doped bismuth oxide quantum dots with evidential *in silico* analysis†

Muhammad Ikram, *[a] Muhammad Shazaib,[b] Ali Haider, [c] Anum Shahzadi,[d] Shair Baz,[a] Mohammed M. Algaradah,[e] Anwar Ul-Hamid, *[f] Walid Nabgan, *[g] Hisham S. M. Abd-Rabboh[h] and Salamat Ali[b]

Herein, Bi_2O_3 quantum dots (QDs) have been synthesized and doped with various concentrations of graphitic carbon nitride (g-C_3N_4) and a fixed amount of carbon spheres (CS) using a co-precipitation technique. XRD analysis confirmed the presence of monoclinic structure along the space group $P2_1/c$ and $C2/c$. Various functional groups and characteristic peaks of (Bi–O) were identified using FTIR spectra. QDs morphology of Bi_2O_3 showed agglomeration with higher amounts of g-C_3N_4 by TEM analysis. HR-TEM determined the variation in the *d*-spacing which increased with increasing dopants. These doping agents were employed to reduce the exciting recombination rate of Bi_2O_3 QDs by providing more active sites which enhance antibacterial activity. Notably, (6 wt%) g-C_3N_4/CS-doped Bi_2O_3 exhibited considerable antimicrobial potential in opposition to *E. coli* at higher values of concentrations relative to ciprofloxacin. The (3 wt%) g-C_3N_4/CS-doped Bi_2O_3 exhibits the highest catalytic potential (97.67%) against RhB in a neutral medium. The compound g-C_3N_4/CS-Bi_2O_3 has been suggested as a potential inhibitor of β-lactamase$_{E.\ coli}$ and DNA gyrase$_{E.\ coli}$ based on the findings of a molecular docking study that was in better agreement with *in vitro* bactericidal activity.

Received 12th July 2023
Accepted 18th August 2023

DOI: 10.1039/d3ra04664h

rsc.li/rsc-advances

1. Introduction

Water is essential in every aspect of life and crucial for all living beings.[1] The Earth's surface contains 71% water; only 0.03% is deemed healthy water when used immediately.[2] The discharge of waste products into freshwater resources, such as organic and inorganic dyes pollutants, must be addressed to sustain a healthy atmosphere.[3] These contaminants cause harm to sea life, terrestrial animals, and plants. Additionally, these contaminants have negative health impacts on humans, such as anemia, bladder discomfort, and gastrointestinal difficulties.[4] The major aquatic contaminants are methyl orange, rhodamine blue (RhB), and methylene blue (MB); the water becomes unsuitable for utilization with these dyes in it.[5] Particularly RhB, a potentially dangerous chemical fluorescent dye used in the biomedical and textile sectors.[6] Another endemic challenge that today's humanity is beginning to encounter is the development of antibiotic resistance in microorganisms. According to the IDSA, the widespread infection of the most potentially fatal species of bacteria known as ESKAPE pathogens possess considerable antibiotic resistance.[7] Annually, *E. coli*, an ESKAPE pathogen, kills 1.3 million children from diarrhea, mainly spreading through contaminated water.[8] Numerous methods have been proposed for dye removal including photocatalysis,[9] adsorption,[10] coagulation,[11] biodegradation,[12] flocculation,[13] micro-electrolysis[14] and catalysis.[15] Among these, catalysis is regarded as an excellent process for the purification of wastewater treatment. Nanomaterial semiconductors are important for catalysis in light of their chemical stability, minimal toxicity, and environmental friendliness.[16]

The Bi-based semiconductor materials such as $BiVO_4$, Bi_2WO_6, Bi_2MoO_6, BiOX (X = Cl, Br and I), and Bi_2O_3 have received a lot of research interest over the past few years owing

[a]*Solar Cell Applications Research Lab, Department of Physics, Government College University Lahore, 54000, Pakistan. E-mail: dr.muhammadikram@gcu.edu.pk*
[b]*Department of Physics, Riphah Institute of Computing and Applied Sciences (RICAS), Riphah International University, 14 Ali Road, Lahore, Pakistan*
[c]*Department of Clinical Sciences, Faculty of Veterinary and Animal Sciences, Muhammad Nawaz Shareef University of Agriculture, Multan 66000, Pakistan*
[d]*Faculty of Pharmacy, The University of Lahore, Lahore 54000, Pakistan*
[e]*Chemistry Department, King Khalid Military Academy, Riyadh 11495, Saudi Arabia*
[f]*Core Research Facilities, King Fahd University of Petroleum & Minerals, Dhahran 31261, Saudi Arabia*
[g]*Departament d'Enginyeria Química, Universitat Rovira i Virgili, Av Països Catalans 26, Tarragona 43007, Spain. E-mail: walid.nabgan@urv.cat*
[h]*Chemistry Department, Faculty of Science, King Khalid University, P.O. Box 9004, Abha 61413, Saudi Arabia*

† Electronic supplementary information (ESI) available. See DOI: https://doi.org/10.1039/d3ra04664h

to their layer structures and high catalytic properties.[17] Among these Bi_2O_3 is frequently used in wastewater treatment. Bi_2O_3 has unique electrical structures that are responsible for the enhancement of absorption. Particularly p-type semiconductor Bi_2O_3 exhibits exceptional features, including a broadband gap, low toxicity, excellent conductivity, antimicrobial activity, and the ability to degrade organic dyes.[18,19] Metal oxides are made more stable and have improved physiochemical characteristics as a result of the inclusion of polymers, leading to effective dye degradation and antibacterial activity.[20]

Pair production occurs when polymers interact with metal ions, which makes them more effective for dye degradation and antimicrobial activity. Various polymers have been used as capping agents and act as inhibitors of the size of material, including polyacrylic acid (PAA), polymethyl methacrylate (PMMA), polyvinylpyrrolidone (PVP), and polyvinyl alcohol (PVA).[21–23] Consequently, a polymeric semiconductor g-C_3N_4 with sp^2 hybridization, a graphite-like structure, with strong C–N bonds and van der Waals forces between the layers exhibits exceptional potential for catalytic degradation, antibacterial activity and many other applications because of low band gap energy, appealing electrical band structure, and good physico-chemical stability. Organic substances like urea, ethylene diamine, and melamine with a nitrogen and carbon bond coupling are frequently paralyzed to the synthesized g-C_3N_4.[24,25] Furthermore, it could be speculated that coupling Bi_2O_3 with g-C_3N_4 forms a heterojunction that promotes charge transfer and separation.[26] Overall CS provides a high surface area, promoting efficient catalysis and enhancing the adsorption of dyes and bacterial cells. The g-C_3N_4 enables the generation of reactive oxygen species (ROS). This combined with the catalytic redox ability of Bi_2O_3 facilitates the degradation of dyes and the production of antibacterial ROS. Moreover, the tunability of these materials allows for customization to meet specific catalytic and antibacterial requirements. Combining these unique properties would enable g-C_3N_4/CS-doped Bi_2O_3 QDs promising material for a wide range of environmental remediation and healthcare applications. The selection of different wt% (3 and 6) of g-C_3N_4 as dopant[27] was adopted from literature, experimental findings, and to attain optimal catalytic and antibacterial outcomes while taking practical feasibility into account.

Herein, the pure and g-C_3N_4/CS-doped Bi_2O_3 QDs were synthesized simultaneously by the co-precipitation method, which was cost-efficient and eco-friendly. Various characterization techniques were utilized to demonstrate the different properties of the synthesized QDs, and the potential for the inhibition of pathogenic microbe *E. coli* and degradation of RhB were investigated.

2. Experimental section

2.1 Materials

The precursor chemical bismuth nitrate pentahydrate ($Bi(NO_3)_3 \cdot 5H_2O$, 98%) was obtained from BDH laboratory supplies. Glucose, g-C_3N_4, and NaOH, 98% were purchased from Sigma-Aldrich Germany.

2.2 Synthesis of CS

The CS were synthesized by employing the hydrothermal carbonization technique. The 1 M of glucose was diluted and stirred continuously to get the transparency of the solution. Finally, the above solution have been taken into an autoclave of stainless steel and kept for 12 h at 180 °C. The final precipitates were dried overnight at 100 °C using an oven after washing them multiple times with deionized (DI) water (Fig. 1a).

2.3 Preparation of g-C_3N_4/CS doped Bi_2O_3

The 0.5 M of ($Bi(NO_3)_3 \cdot 5H_2O$) was used to prepare Bi_2O_3 with continuous stirring and heating at 100 °C for 30 min. 1 M NaOH was added dropwise for the formation of precipitates and to maintain pH ~12. The prepared solution was washed thrice using a centrifuge at 7000 rpm and left on a hotplate at 150 °C for 12 h. Afterward, dried QDs have been pulverized nicely, and using the same method, the (3 and 6 wt%) of g-C_3N_4 and a fixed amount of CS, doped Bi_2O_3 QDs were prepared as depicted in Fig. 1b.

2.4 Catalysis

The CA for degradation of RhB using bare and doped Bi_2O_3 was analyzed to ensure the reliability of the experimental findings. The reagents such as $NaBH_4$ and RhB have been prepared freshly. The RhB solution of A 10 mg L^{-1} was equally distributed into three parts having the pH (pH = 4), (pH = 7), and (pH = 12), for acidic, neutral, and basic mediums respectively.[28] 400 μL of $NaBH_4$ and 3 mL of the dye were combined and 400 μL of synthesized QDs solution (like Bi_2O_3 and g-C_3N_4/CS-Bi_2O_3) was added in a $NaBH_4$ and RhB aqueous solution. A catalyst had been employed to limit the reaction's surface activation energy, which improved the stability and effectiveness of the reaction. A UV-vis spectrophotometer was used to assess the degree of dye degradation in the produced supernatant over a period of time and at 554 nm RhB emits its absorption signal.[29] The color of RhB changes from pink to colorless as a result of the reduction and the % degradation has been calculated using the formula.

$$\%\ \text{degradation} = \frac{C_0 - C_t}{C_0} \times 100$$

2.5 Isolation and identification of *E. coli*

2.5.1 Sample collection and isolation. Prompt milking in a sterilized glass container was utilized to collect the samples of unpasteurized milk from various dairy sheep, veterinary hospitals, and local farms in south Punjab, (Pakistan). The temperature of milk samples was maintained at 4 °C during transportation. MacConkey agar was employed for determining the coliform pathogen found in that milk and the plates were incubated at 36 °C for 48 h.

2.5.2 Identification and characterization of bacterial isolates. The microorganism *E. coli* was selected as a model for bactericidal investigation. Its identification was based on the colonial morphology complying with several biochemical tests,

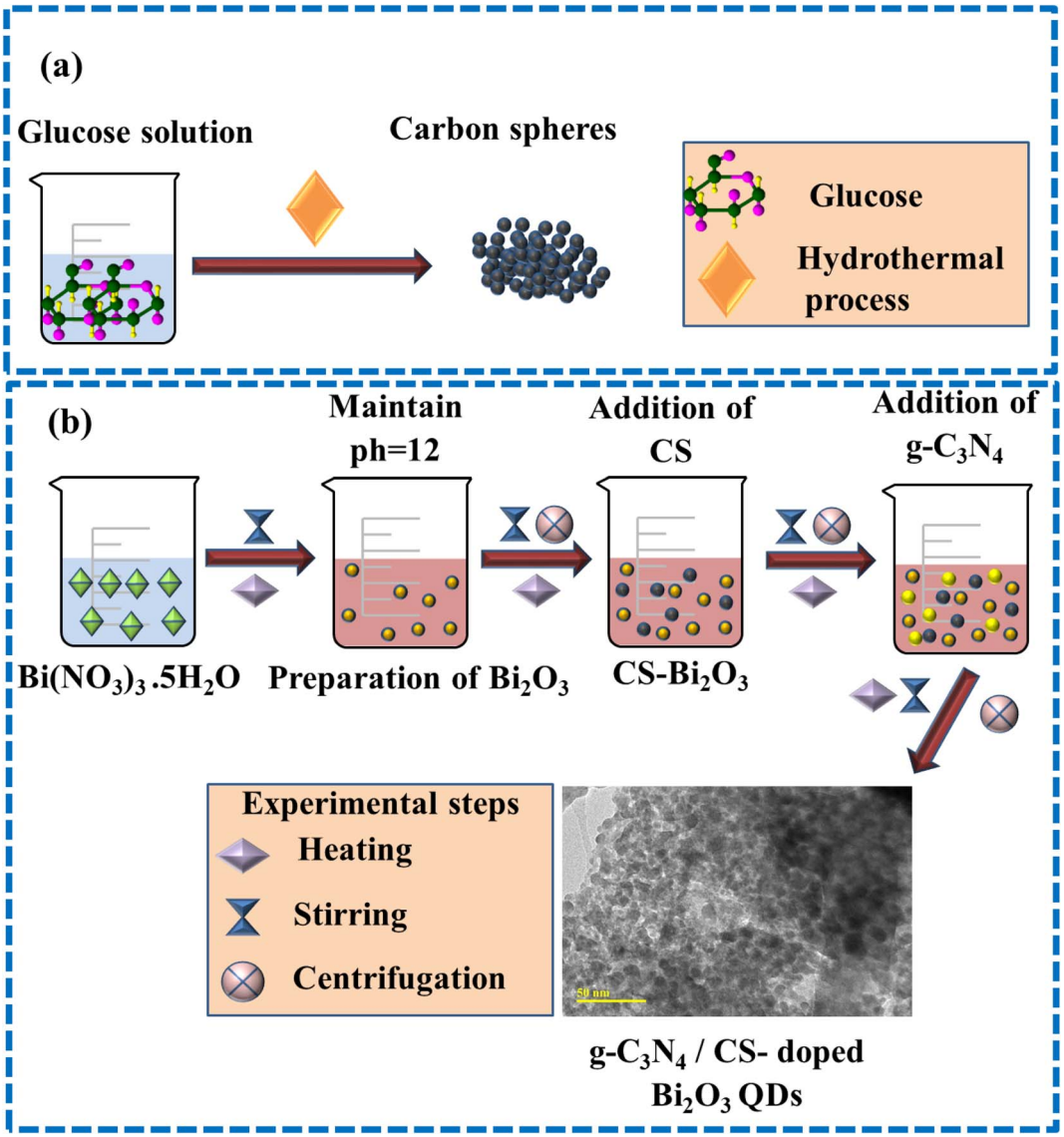

Fig. 1 (a and b) Synthesis of g-C_3N_4 and CS doped Bi_2O_3 QDs.

Gramm staining, and referencing Bergey's manual of determinative bacteriology.[30]

2.5.2.1 Antibiotic susceptibility. To examine antibiotic susceptibility, Kirby–Bauer test was employed on Mueller Hinton agar (MHA).[31] The antimicrobial tests against the antibiotics such as tetracycline (Te) 30 μg (tetracyclines), azithromycin (Azm) 15 μg (macrolides), ciprofloxacin (Cip) 5 μg (quinolones), amoxicillin (A) 30 μg (penicillin), imipenem (Imi) 10 μg (carbapenem), ceftriaxone (Cro) 30 μg (cephalosporins) and gentamicin (Gm) 10 μg (aminoglycosides) were performed to observe the *E. coli's* resistance.[32] The purified *E. coli* cultures were subjected to growth until they reached (0.5) MacFarland standard for turbidity and the spread plate had been placed on growth medium MHA (Oxoid Limited, Basingstoke, UK). To avoid inhibition zone overlap, the discs were placed apart from the infected plate and the antibiotic plates were cultured at 36 °C for 24 h. The results were examined under the guidelines of the Clinical, Diagnostic, and Laboratory Standard Institute.[33]

2.5.2.2 Antimicrobial activity. In vitro, the antibacterial capability was assessed *via* determining the inhibition zone of pristine and doped Bi_2O_3 against isolates of MDR *E. coli*. *E. coli* has been isolated on MacConkey agar plates of (0.5) McFarland standards 1.5×10^8 CFU μL^{-1}. The potentially harmful bacterial drugs have been sanitized by agar plates. The cork borer was utilized for drilling holes having a diameter of 6 millimeters (mm). Ciprofloxacin 5 mg/50 mL functions as the positive control while DI water 50 mL serves as the negative control. The bare and doped QDs were injected into the boreholes at low and high concentrations (0.5 mg/50 μL and 1.0 mg/50 μL). The capability of the QDs to suppress the growing process of microorganisms was measured by determining the expansion of the inhibition zone using a Vernier caliper.

2.5.2.3 Statistical analysis. To perform the preliminary identification of the effectiveness of antimicrobials, zones of inhibition were utilized, and the diameters of these zones have

been analyzed statistically using one-way analysis of variance (ANOVA) in SPSS 20.[34]

2.6 Molecular docking study

The binding affinity of g-C_3N_4/CS-Bi_2O_3 QDs with specific enzyme targets was investigated. Based on the microbicidal activity of the synthesized QDs against *E. coli*, β-lactamase and DNA gyrase from *E. coli* were selected, and the binding strength within their respective active sites was evaluated. β-Lactamase$_{E. coli}$ and DNA gyrase$_{E. coli}$ structural dimensions were derived from the protein data bank using accession codes 4KZ3 (Res: 1.67 Å)[35] and 6KZX (Res: 2.1 Å),[36] respectively. The software SYBYL-X 2.0 was used for docking research. In a previous study[37,38] SYBYL-X 2.0 was used to construct three-dimensional structures of pharmaceuticals and to evaluate the binding affinities of QDs with active site residues of designated proteins.

3. Results and discussion

X-ray diffraction (XRD) technique was utilized for the analysis of phase composition and crystallinity of bare and doped Bi_2O_3 QDs (Fig. 2a). Diffraction peaks in the range of 2θ (20–60°) appearing at 29.50° ($\bar{3}11$), 33.04° ($\bar{1}22$), 35.05° (020), 38.39° ($\bar{3}12$), and 47.57° (140) revealed the monoclinic structure along the space group $P2_1/c$ and $C2/c$, well matched with the JCPDS files (01-083-0410/00-041-1449). The distinctive peaks of amorphous CS were observed at about 23.8° (002) and 44° (101) (Fig. 2a).[39] The minor shift and the increase in peak intensities were ascribed to the significant dispersion of the CS between the host interlayers. Additionally, larger crystallites are given a specific crystal plane, resulting in more intense peaks in the XRD pattern.[40] The characteristic peaks of g-C_3N_4 could not be observed ascribed to the small trace amount or low crystallinity, however, the peak intensities decrease gradually with an increasing percentage of g-C_3N_4.[41] FTIR spectra of pristine and doped Bi_2O_3 QDs were analyzed to determine functional groups and vibrational modes can be seen in Fig. 2b. The FTIR spectra have a functional group region, ranging from 4000 to 1500 cm^{-1} and the zone of fingerprint can be observed between 1500 and 400 cm^{-1}. The band observed at 3200–3400 is referred to as the characteristic vibrations of the O–H group.[42] The band at 1640 cm^{-1} corresponds to the symmetry stretching vibration of the C=O bond (in –COOH).[43] The stretching vibrations of Bi–O–Bi and C–C were attributed to 540 and 1090 cm^{-1} bands, correspondingly.[44,45] Furthermore, the 519 cm^{-1} band corresponds to the vibrations of Bi–O bonds, confirming the presence of the Bi_2O_3 QDs.[46] The g-C_3N_4 introduction into CS-Bi_2O_3 results in forming a new mid-gap hybrid of p states, enhancing the infrared absorption capability. However, a higher level of g-C_3N_4 doping resulted in a decrease in infrared absorption due to band position changes and defects in the crystalline structure.[47] The polycrystalline nature of Bi_2O_3, CS-Bi_2O_3, and (3 and

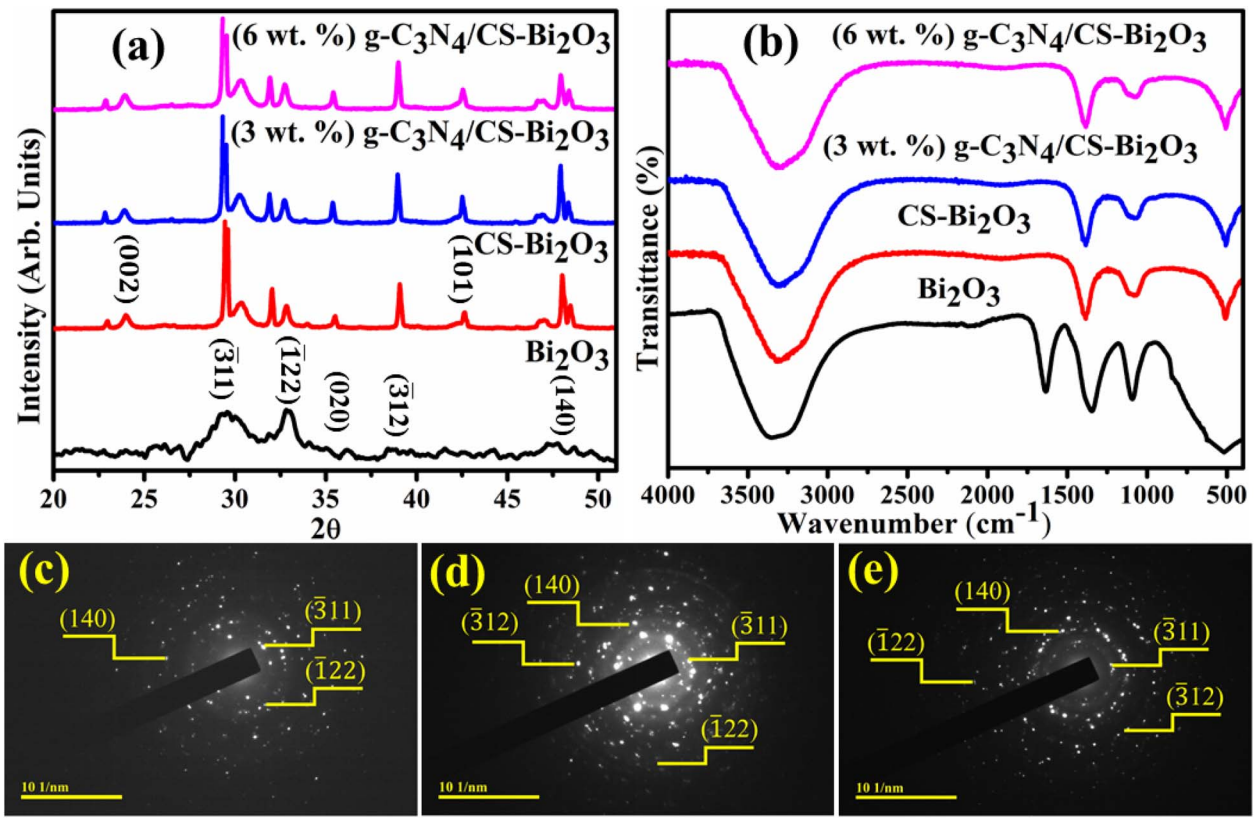

Fig. 2 (a) XRD patterns, (b) FTIR spectra of pure and (3 and 6 wt%) g-C_3N_4/CS-doped Bi_2O_3 and (c–e) SAED images of pristine and CS-Bi_2O_3 and (3 wt%) g-C_3N_4 doped Bi_2O_3.

6 wt%) g-C_3N_4/CS-doped Bi_2O_3 QDs was confirmed with distinct rings and bright spots of SAED images. The circular rings were harmonized with the plans ($\bar{3}11$), ($\bar{1}22$), (140), and (312) of XRD (Fig. 2c–e).

The optical absorption characteristics of the synthesized Bi_2O_3 and (3 and 6 wt%) g-C_3N_4/CS-doped Bi_2O_3 have been assessed by employing an ultra-visible spectrophotometer by encompassing the wavelength range of 230–450 nm (Fig. 3a). The λ_{max} of Bi_2O_3 was observed at 295 nm was ascribed to the π–π* transition due to the functional groups (such as OH, >C=O).[48,49] Tauc's equation revealed the energy band gap of 4.2, 4.16, 3.54 and 3.97 eV for bare and doped QDs, respectively.[50] The reduction in band gap energy from 4.2 to 3.54 eV with the incorporation (3 wt%) g-C_3N_4/CS-doped Bi_2O_3 caused improvement in the catalytic activity as the catalyst structure, surface area, and crystallite size have each a substantial impact on its catalytic activity.[51] Furthermore, redshift was associated with particle size growth and the quantum size impact of QDs.[52]

The PL spectra of the doped and undoped Bi_2O_3 were examined in the 400–580 nm regions. Bi_2O_3 QDs exhibit peaks in the visible spectrum ranging from 520 to 540 nm, corresponding to the presence of Bi^{3+} ions when excited at 300 nm.[53] Another peak of Bi_2O_3 has been observed at 410–430 nm (Fig. 3b) and was matched with previous work.[54] The decreased PL emission intensity of the synthesized Bi_2O_3 QDs upon the doping of CS and g-C_3N_4 was attributed to the reduction in the excitation recombination rate. Peak intensity was significantly decreased with the incorporation of (3 wt%) g-C_3N_4 compared to bare and (6 wt%) g-C_3N_4/CS-doped Bi_2O_3 QDs that suggests the tendency of high recombination rate of photo-generated charge carriers.[55] According to prior research outcomes, lower peak intensity suggests increased surface vacancies of oxygen, resulting in improved catalytic efficiency.

The elemental compositions of prepared QDs were investigated using EDS analysis. The occurrence of Bi and O strong peaks confirms the presence of Bi_2O_3 QDs, gold peaks were the outcome of the coating sprayed for reducing charging effects, and NaOH produced the sodium peak used for maintaining the pH of the samples (Fig. S1(a)†). The smaller peaks of zinc and copper were caused by the presence of some contaminants and the brass sample holder used throughout the EDS analysis. Furthermore, the increase in the wt% of O denotes the presence of dopants (Fig. S1(b–d)†).

TEM analysis has been employed to examine the topography and morphology of prepared QDs (Fig. 4a–d). The Bi_2O_3 sample revealed multiple morphologies as few nanorods with the QDs were observed (Fig. 4a). The chunk-like morphology appeared with a higher degree of agglomeration of QDs. The addition of CS into Bi_2O_3 showed that the agglomerated QDs anchored with carbon sphere can be seen (Fig. 4b). The incorporation of g-C_3N_4 into the binary system of CS-Bi_2O_3 showed that QDs linked to CS and g-C_3N_4 each other forming a network may facilitate to charge carriers movement participate in dye degradation (Fig. 4c). With a higher concentration of g-C_3N_4, the agglomeration increased seems that as overlapped by C_3N_4 nanosheets to QDs anchored with CS (Fig. 4d). Gatan software was additionally employed to compute interlayer *d*-spacing from HR-TEM images (Fig. S2(a–d)†). The average *d*-spacing values for the Bi_2O_3 and (3 and 6 wt%) g-C_3N_4/CS-doped Bi_2O_3 QDs were determined to be 0.250, 0.266, 0.293 and 0.292, which are all under the XRD data. Furthermore, the variation in the lattice spacing of Bi_2O_3 among distinct materials was corroborated by TEM findings.

The monoclinic structure within the space groups $P2_1/c$ and $C2/c$ of bare and doped Bi_2O_3 QDs in the 2θ range (20–60°) was determined using the Analytical XPert PRO X-ray diffraction system. The FTIR spectra identified the stretching vibrations of Bi–O–Bi and C–C vibrations of Bi–O bonds, confirming the presence of Bi_2O_3 quantum dots. The λ_{max} of Bi_2O_3, encompassing the wavelength range of 230–450 nm, was investigated through a UV-vis spectrophotometer to study π–π* transitions attributed to functional groups. The existence of Bi^{3+} ions and the excitation recombination rate of pure and doped Bi_2O_3 QDs were determined using PL spectra. Strong Bi and O peaks,

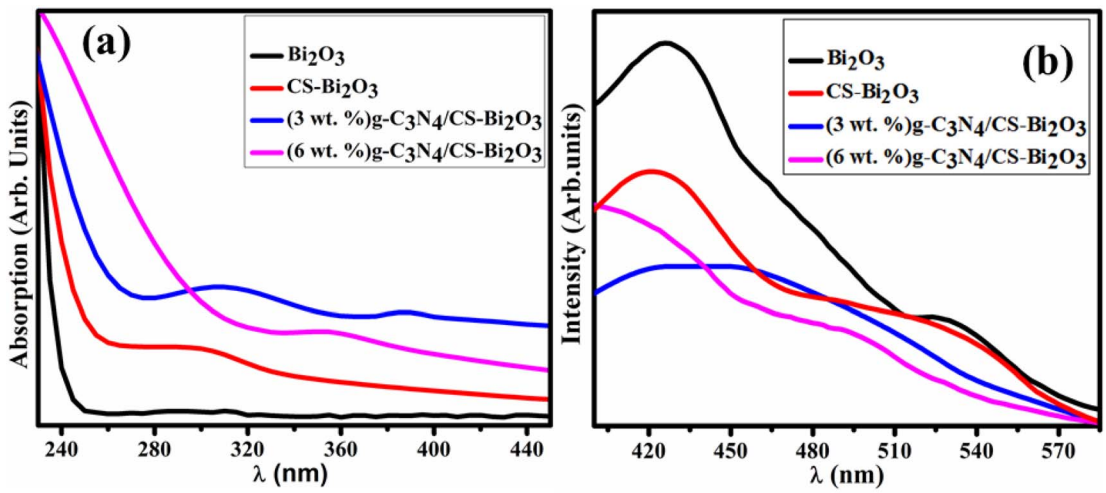

Fig. 3 (a) UV-vis reflectance spectra (b) PL spectra of Bi_2O_3, CS-Bi_2O_3 (3 wt%) g-C_3N_4/CS-Bi_2O_3 and (6 wt%) g-C_3N_4/CS-Bi_2O_3 respectively.

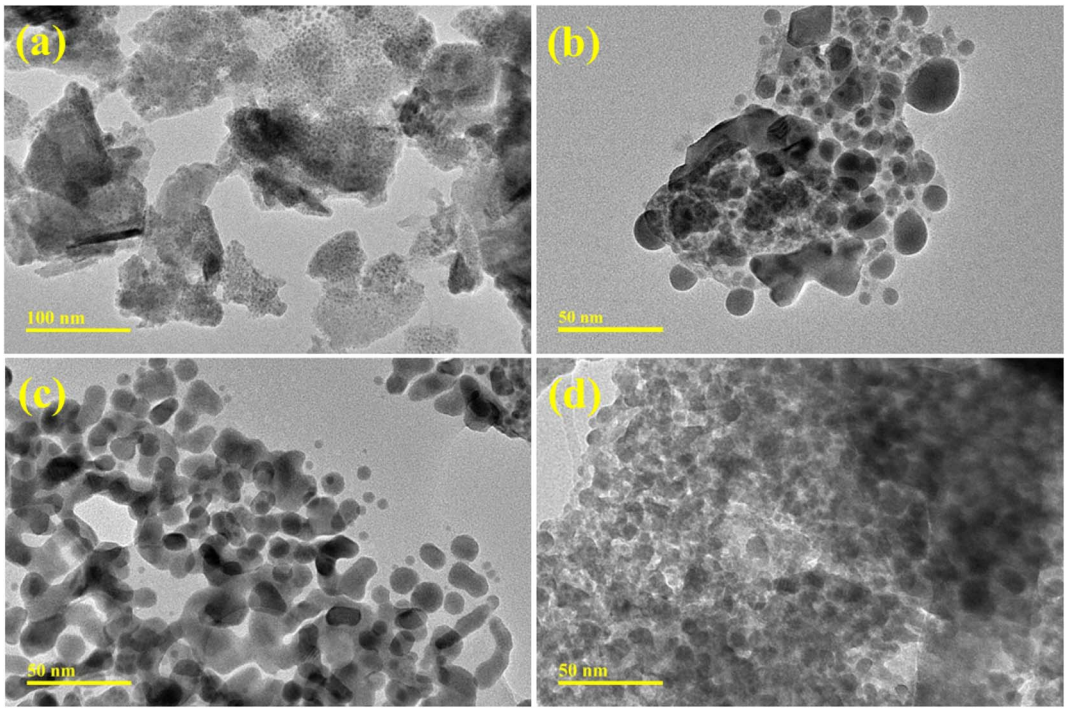

Fig. 4 TEM images of (a) Bi_2O_3 (b) CS-Bi_2O_3 (c) (3 wt%) g-C_3N_4/CS-doped Bi_2O_3 (d) (6 wt%) g-C_3N_4/CS-doped Bi_2O_3 QDs.

indicating the presence of Bi_2O_3 QDs, EDS. TEM images shows that the incorporation of g-C_3N_4 into CS-Bi_2O_3 binary system creates a network, where QDs interconnect with CS and g-C_3N_4. This network enhances charge carrier mobility, contributing to efficient dye degradation.[56] For the measurement of inter-planar *d*-spacing values, high-resolution transmission electron microscopy was employed.

CA of Bi_2O_3 and (3 and 6 wt%) g-C_3N_4/CS-Bi_2O_3 QDs for RhB dye in different pH mediums with the inclusion of $NaBH_4$ was measured using UV-vis spectrophotometer. The bare and doped catalyst showed maximum degradation of 49.69, 84.36, 94.38, and 80.96% in acidic medium (pH = 4) 58, 83.09, 70.72, and 92.54% in basic medium (pH = 11) 60.21, 97.13, 97.67, and 95.65% at pH = 7 respectively for 5 min as revealed in Fig. 5a–c. CS-doped Bi_2O_3 sample showed enhanced catalytic activity in neutral basic and acidic mediums respectively. The CS-doped Bi_2O_3 catalyst exhibited a higher degradation rate due to the pristine material may not have the same effects on interfacial charge transfer or the trapping of electrons.[57] CS acts as a dispersing support, preventing Bi_2O_3 particle agglomeration.[58] Second, this reduces the band gap, increases the absorption range and CS plays a crucial role in enhancing the electron transport characteristics of Bi_2O_3;[59] hence the CS-doped Bi_2O_3 shows enhanced catalytic activity as compared to the bare catalyst. The (3 wt%) g-C_3N_4/CS-doped Bi_2O_3 exhibits higher degradation efficiency at the natural pH of the RhB aqueous solution because g-C_3N_4 reduces charge recombination and increases the interfacial contact between the catalyst and the RhB.[59] Furthermore, the increasing wt% of the g-C_3N_4 causes a decrease in the degrading efficiency because the higher doping of g-C_3N_4 may block the active sites and reduce the separation efficiency of the generated charges.[60] It is challenging to assess the impact of pH on the efficiency of the catalytic degradation of organic molecules due to its diverse functions. In the context of three distinct aqueous mediums ranging from acidic to neutral, the catalytic efficiency of (6 wt%) g-C_3N_4/CS-doped Bi_2O_3 approached maximal levels, exhibiting a range between 80 and 95%. The optimum conditions for the catalyst to produce hydroxyl radicals, the most active species for RhB degradation, were probably responsible for a higher degradation efficiency at the natural pH of RhB.[61] In addition to the collapse of the catalyst structure, electrostatic repulsion and the adsorption capacity of (6 wt%) g-C_3N_4/CS-doped Bi_2O_3 was dramatically reduced under basic to strong acid conditions.[62] As a consequence of an increase in the OH-concentration, which more oxidizes RhB, the CA in the basic medium was higher than acidic but lower than neutral. It was caused by the OH^- ions of the basic solution neutralizing the H^+ ions on the catalyst surface.[63]

The catalytic mechanism of QDs was illustrated in Fig. S3,† the nanocatalyst and reducing agent play important role in dye degradation. The QDs help improve reaction speed and stability and lower the activation energy through electron transfer between the donor BH_4- and acceptor RhB, commonly referred to as the electron relay effect. The degradation has been influenced by the catalyst surface size, area, and shape which provide more active sites, resulting in the reduction of RhB to Leuco (LRhB) by efficiently breaking down molecules while the OH^- ions were produced. With the addition of nanocatalyst adsorption occurs and the $NaBH_4$ had been dissociated into

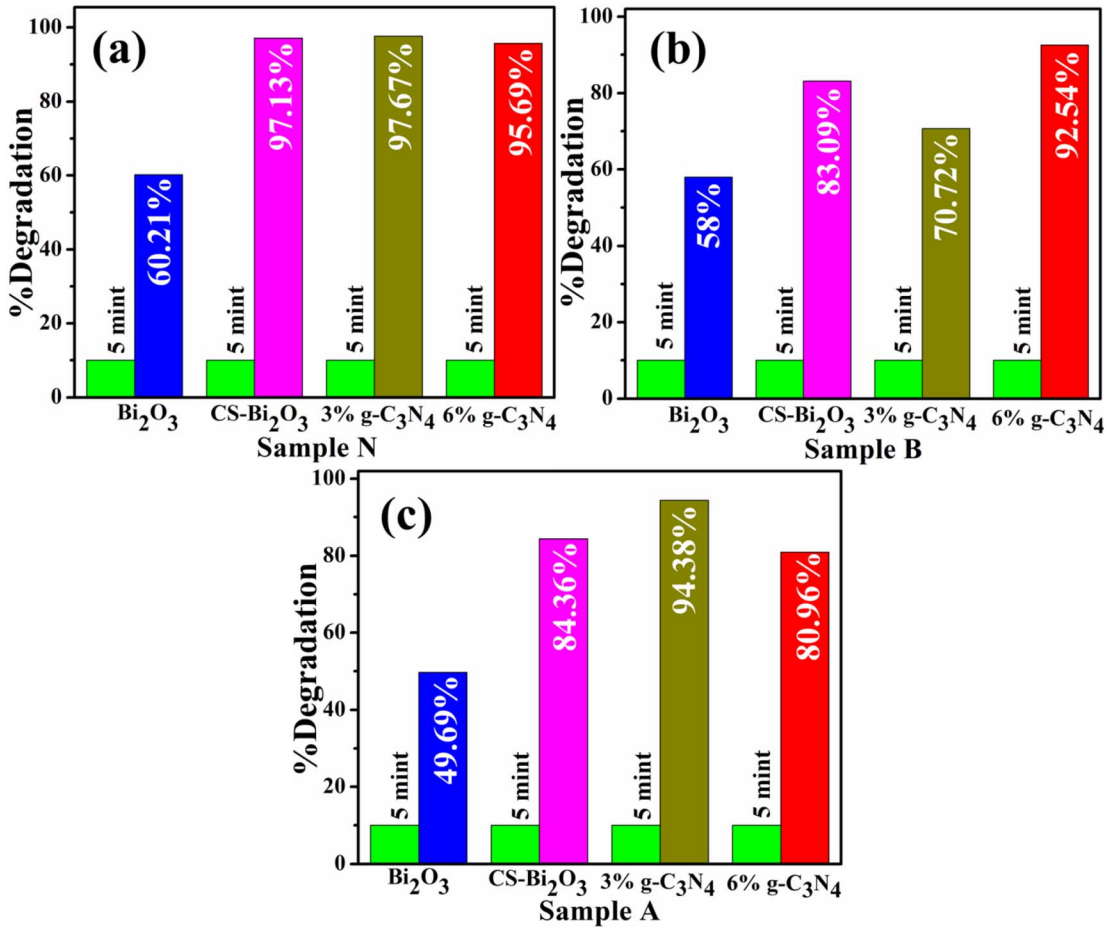

Fig. 5 Catalytic activity of pristine and (3, 6 wt%) g-C_3N_4/CS-Bi_2O_3 in (a) neutral medium (b) basic medium, and (c) acidic medium.

BH_4^- while more ions diffused onto the surface. QDs accelerated the adsorption of BH_4^- ions and the molecules of dye across numerous active sites, causing the dye to degrade more rapidly and effectively.[64] With the small size and larger surface area, the catalyst has more active sites, which increases its catalytic activity. If the catalyst has a wide surface area, microporosity limits the active sites, which leads the degrading efficiency to drop. Without a catalyst, the reaction proceeds slowly, while adding a catalyst speeds up the dye degradation.[65]

The agar well diffusion method has been employed to assess the bactericidal potential of the pristine and (3 and 6 wt%) g-C_3N_4/CS-doped Bi_2O_3 QDs against *E. coli*. Significant inhibitory zones have been assessed by the regions 0–1.95 mm and 0.60–2.85 mm for low and high concentrations, respectively, as lower and higher concentrations against *E. coli* as mentioned in Table 1 QDs were placed in the appropriate wells; meanwhile the ciprofloxacin for comparison 7.25 mm and DI water having 0 mm evaluation of the inhibition zone was used as a positive and negative control respectively. At the lower concentrations, bare specimens captured no inhibition zones throughout the measurements, while the Bi_2O_3 loaded with CS and (3, 6 wt%) g-C_3N_4 exhibits a considerable number of inhibition zones. The (6 wt%) g-C_3N_4/CS-doped Bi_2O_3 QDs demonstrated enhanced antibacterial efficacy (1.95–2.85) at lower and higher concentrations owing to alterations in the membrane structure of the bacteria.

Table 1 Inhibition zone at low and high concentrations for *E. coli* bacteria

Samples	*E. coli* inhibition zone (mm)			
	0.5 mg/50 μL	1.0 mg/50 μL	Ciprofloxacin	Deionized water
Bi_2O_3	0	0.60	7.25	0
CS-Bi_2O_3	0.90	2.05	7.25	0
(3 wt%) g-C_3N_4/CS-Bi_2O_3	1.45	2.25	7.25	0
(6 wt%) g-C_3N_4/CS-Bi_2O_3	1.95	2.85	7.25	0

The interaction of the material with bacteria cells to block the transport chain and the negatively charged surface of Gram-negative bacteria with a strong affinity for positive ions facilitates electrostatic interactions between QDs and the bacterial surface. As a result, antimicrobial agent can directly cross the cell membrane and disturb cell function (Fig. S2†). The hydroperoxyl radical ($*HO_2$) is formed when superoxide anion radicals (O^{2-}) combine with H^+ ions. The hydrogen peroxide radical ($*H_2O_2$) develops when the hydroperoxyl radical ($*HO_2$)

interacts with e^- and H^+. The QDs promote single and dual-wrecked breaks inside the nucleic acid base of nitrogen and sugar-phosphate link' by the production of intracellular ROS that interact with the nucleic acid inside the bacterial cell.[66] This is performed by encouraging the oxidation of residual amino acids and disconnecting critical proteins, so interfering with numerous metabolic operations.[67] As a result, ROS damaged nucleic acid and was thought to be responsible for DNA breakage, consequently leading to bacterial death.[68] The interaction of an enormous electrostatic charge (Bi^{3+}) and a bacterial membrane cause lysis and cell collapse. This contact eventually results in the death of the microorganisms involved. Table 1 shows that at the higher concentration of the QDs, the ability to destroy bacteria was increased.[67]

The capacity of computational methods, especially molecular docking studies, to permit in-depth examination of mechanisms underlying varied biological traits has garnered them substantial attention in recent decades. Using a molecular docking methodology, the suggested approach evaluated the binding capacity and inhibitory potential of synthesized QDs to identify optimal enzyme inhibitors. Antibiotic research has focused heavily on two enzymes-β-lactamase and DNA gyrase, that play critical roles in bacterial growth and survival.[69] In the instance of β-lactamase$_{E.\ coli}$, binding scores of 3.48, 3.79, and 7.01 for Bi_2O_3, CS-Bi_2O_3, and g-C_3N_4/CS-Bi_2O_3 QDs, respectively, indicated an acceptable binding propensity within the active pocket where Bi_2O_3 formed hydrogen bonds with Ser212 and Gly320. The H-bonding patterns of CS-Bi_2O_3 with Gln120, Asn152, and Asn343 are represented in Fig. 6b and c, whereas the H-bonding patterns of g-C_3N_4/CS-Bi_2O_3 with Gln120, Arg148, Ala318, and Thr316 are depicted in Fig. 6d.

The active pocket of DNA gyrase (a common target for antibiotics) was also used to build and study docking complexes. The best binding scores (2.93 and 3.34, respectively) were found for docked complexes including Bi_2O_3 and CS-Bi_2O_3, both of which formed H-bonds with Thr165 (Fig. 7a–c). Fig. 7d shows that g-C_3N_4/CS-Bi_2O_3 showed four H-bonds, with Asn46, Asp73, Arg136, and Thr165 all having a binding score of 3.91.

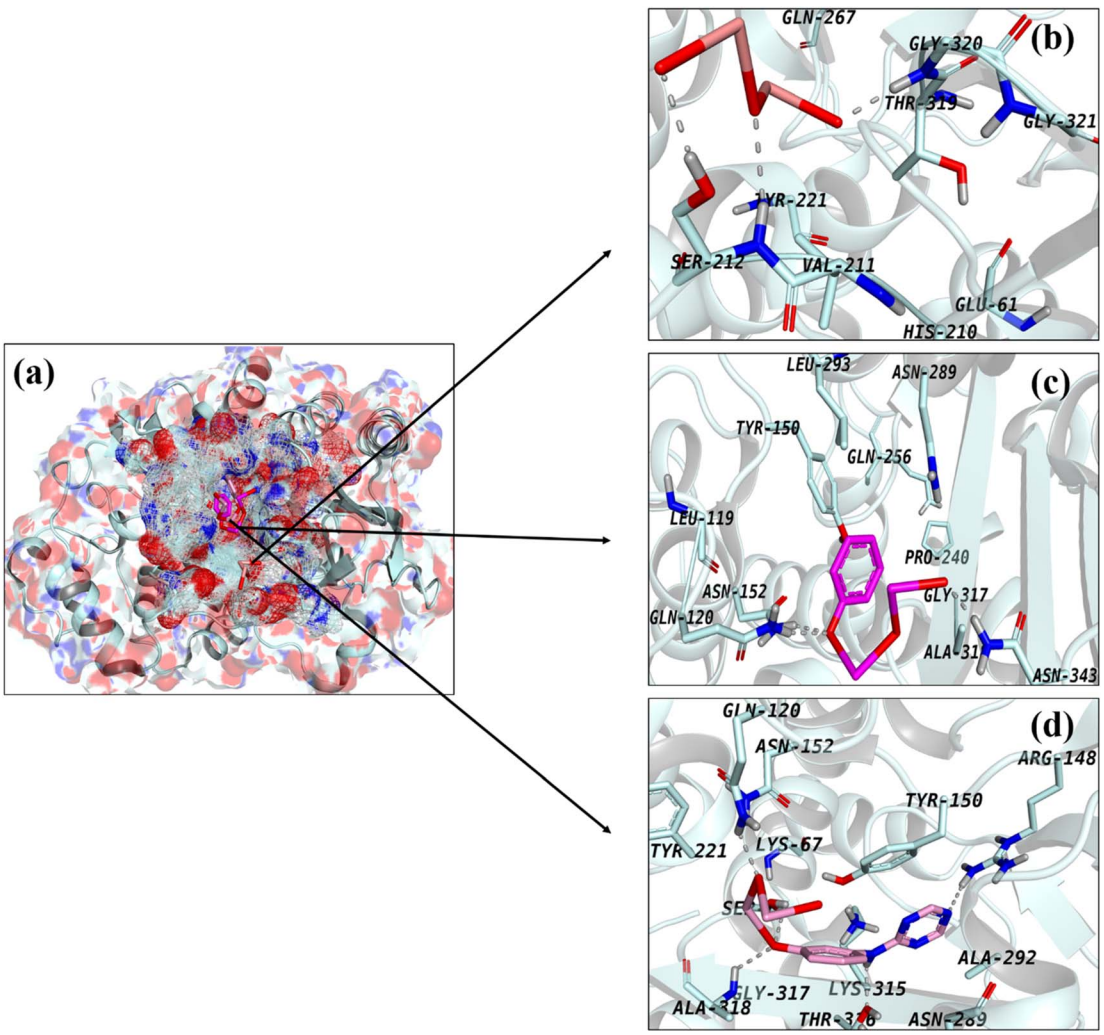

Fig. 6 Binding interaction pattern of (a) superimposed complexes, (b) Bi_2O_3, (c) CS-Bi_2O_3, and (d) g-C_3N_4/CS-Bi_2O_3 QDs inside active pocket of β-lactamase$_{E.\ coli}$.

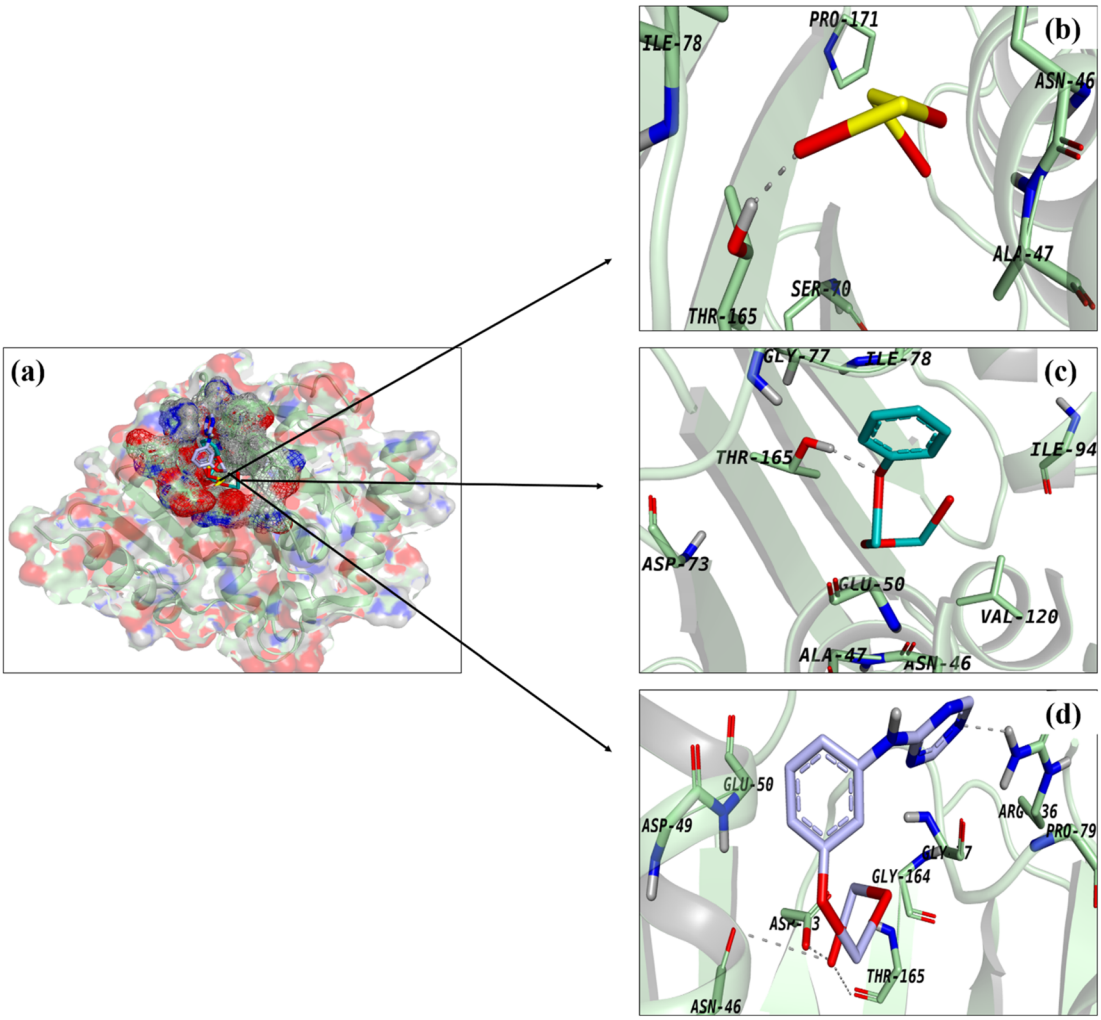

Fig. 7 Binding interaction pattern of (a) superimposed complexes, (b) Bi_2O_3, (c) CS-Bi_2O_3 and (d) g-C_3N_4/CS-Bi_2O_3 QDs inside active pocket of DNA Gyrase$_{E.\ coli}$.

4. Conclusion

In this study, g-C_3N_4/CS-Bi_2O_3 QDs were effectively synthesized using an eco-friendly, cost-effective co-precipitation approach. The XRD pattern and sharp peaks confirmed the monoclinic structure of synthesized QDs were observed upon doping. The existence of the Bi–O–Bi stretching vibration at 540 cm^{-1} of the synthesized QDs confirmed by FTIR moreover, the presence of Bi_2O_3 was confirmed with EDS. The calculated band gap energies were found from 4.2 to 3.54 eV showing decreasing trend upon doping. Peak intensity dropped after CS and g-C_3N_4 doping, indicating a lower charge-to-hole recombination rate, but the higher dose of g-C_3N_4 indicates enhanced charge-to-hole recombination. TEM analysis exhibits the QDs morphology of Bi_2O_3, and agglomeration has been observed upon doping (6 wt%) g-C_3N_4. HRTEM images were utilized to calculate the interlayer spacing (0.272, 0.279, 0.279, and 0.276 Å), which was in satisfactory agreement with XRD data. Molecular docking verified synthesized QDs as possible inhibitors of β-lactamase and DNA gyrase enzymes, demonstrating their efficacy against Gram-negative bacteria. As research progresses, this finding will pave the way for generating binary-doped heterostructures with applications in dye degradation and a potential candidate for killing the microorganisms.

Conflicts of interest

No conflict of interest.

Acknowledgements

The authors extend their appreciation to the Deanship of Scientific Research at King Khalid University, Saudi Arabia, for funding this work through Large Groups Project under grant number (RGP.2/228/44).

References

1 A. A. Yaqoob, T. Parveen, K. Umar and M. N. Mohamad Ibrahim, *Water*, 2020, **12**, 495.

2 Y. Hu and H. Cheng, *Environ. Dev.*, 2013, **8**, 57–73.
3 M. Nasrollahzadeh, M. Sajjadi, S. Iravani and R. S. Varma, *J. Hazard. Mater.*, 2021, **401**, 123401.
4 P. Chowdhary, R. N. Bharagava, S. Mishra and N. Khan, in *Environmental Concerns and Sustainable Development: Volume 1: Air, Water and Energy Resources*, ed. V. Shukla and N. Kumar, Springer Singapore, Singapore, 2020, pp. 235–256, DOI: 10.1007/978-981-13-5889-0_12.
5 H. Saeed, M. Ikram, A. Haider, S. Naz, A. Ul-Hamid, W. Nabgan, J. Haider, S. M. Ibrahim, H. Ullah and S. Khan, *Surf. Interfaces*, 2023, **38**, 102804.
6 S.-M. Hasheminya and J. Dehghannya, *Part. Sci. Technol.*, 2020, **38**, 1019–1026.
7 S. Santajit and N. Indrawattana, *BioMed Res. Int.*, 2016, **2016**, 2475067.
8 Y. Zhang, W. Xiu, S. Gan, J. Shan, S. Ren, L. Yuwen, L. Weng, Z. Teng and L. Wang, *Front. Bioeng. Biotechnol.*, 2019, **7**, 218.
9 H. Kiwaan, T. Atwee, E. Azab and A. El-Bindary, *J. Mol. Struct.*, 2020, **1200**, 127115.
10 A. H. Jawad, A. S. Abdulhameed and M. S. Mastuli, *J. Taibah Univ. Sci.*, 2020, **14**, 305–313.
11 S. Ihaddaden, D. Aberkane, A. Boukerroui and D. Robert, *J. Water Process Eng.*, 2022, **49**, 102952.
12 L. Ayed, K. Chaieb, A. Cheref and A. Bakhrouf, *Desalination*, 2010, **260**, 137–146.
13 J.-H. Deng, X.-R. Zhang, G.-M. Zeng, J.-L. Gong, Q.-Y. Niu and J. Liang, *Chem. Eng. J.*, 2013, **226**, 189–200.
14 S. Wang, S. Tang, H. Yang, F. Wang, C. Yu, H. Gao, L. Fang, G. Sun, Z. Yi and D. Li, *J. Mater. Sci.: Mater. Electron.*, 2022, **33**, 7172–7190.
15 M. Ikram, A. Rafiq Butt, A. Fatima, I. Shahzadi, A. Haider, A. Ul-Hamid, T. Alshahrani and W. Nabgan, *J. Photochem. Photobiol., A*, 2023, **443**, 114835.
16 I. M. Hamouda, *J. Biomed. Res.*, 2012, **26**, 143–151.
17 Q. He, Y. Ni and S. Ye, *RSC Adv.*, 2017, **7**, 27089–27099.
18 H. Sudrajat and P. Sujaridworakun, *Mater. Des.*, 2017, **130**, 501–511.
19 S. S. Raut, O. Bisen and B. R. Sankapal, *Ionics*, 2017, **23**, 1831–1837.
20 Z. B. Shifrina, V. G. Matveeva and L. M. Bronstein, *Chem. Rev.*, 2019, **120**, 1350–1396.
21 S. F. Bdewi, O. G. Abdullah, B. K. Aziz and A. A. R. Mutar, *J. Inorg. Organomet. Polym. Mater.*, 2016, **26**, 326–334.
22 A. Biswal, P. K. Sethy and S. K. Swain, *Polym.-Plast. Technol. Mater.*, 2021, **60**, 182–194.
23 N. Rouabah, B. Boudine, R. Nazir, M. Zaabat, A. S. Alqahtani, M. S. Alqahtani and R. Syed, *J. Polym. Res.*, 2021, **28**, 1–10.
24 T. V. Surendra, C. S. Espenti and S. V. Arunachalam, in *Nanostructured, Functional, and Flexible Materials for Energy Conversion and Storage Systems*, Elsevier, 2020, pp. 325–343.
25 N. Murugasenapathi and P. Tamilarasan, in *Nanoscale Graphitic Carbon Nitride*, Elsevier, 2022, pp. 515–544.
26 G. Fan, Z. Ma, X. Li and L. Deng, *Ceram. Int.*, 2021, **47**, 5758–5766.
27 P. Mary Rajaitha, K. Shamsa, C. Murugan, K. B. Bhojanaa, S. Ravichandran, K. Jothivenkatachalam and A. Pandikumar, *SN Appl. Sci.*, 2020, **2**, 572.
28 H. Ullah, E. Viglašová and M. Galamboš, *Processes*, 2021, **9**, 263.
29 R. Vijayan, S. Joseph and B. Mathew, *Particulate Science and Technology*, 2018.
30 C. G. Sinclair, *Am. J. Trop. Med. Hyg.*, 1939, **1**, 605–606.
31 A. Bauer, *Am. J. Clin. Pathol.*, 1966, **45**, 493–496.
32 F. Adzitey, S. Yussif, R. Ayamga, S. Zuberu, F. Addy, G. Adu-Bonsu, N. Huda and R. Kobun, *Microorganisms*, 2022, **10**, 1335.
33 M. A. Wikler, *Performance Standards for Antimicrobial Susceptibility Testing, Sixteenth Informational Supplement, M100-S16*, Clinical and Laboratory Standards Institute (CLSI), Pennsylvania, 2006, vol. 26(3).
34 A. Haider, M. Ijaz, S. Ali, J. Haider, M. Imran, H. Majeed, I. Shahzadi, M. M. Ali, J. A. Khan and M. Ikram, *Nanoscale Res. Lett.*, 2020, **15**, 1–11.
35 S. Barelier, O. Eidam, I. Fish, J. Hollander, F. Figaroa, R. Nachane, J. J. Irwin, B. K. Shoichet and G. Siegal, *ACS Chem. Biol.*, 2014, **9**, 1528–1535.
36 F. Ushiyama, H. Amada, T. Takeuchi, N. Tanaka-Yamamoto, H. Kanazawa, K. Nakano, M. Mima, A. Masuko, I. Takata and K. Hitaka, *ACS Omega*, 2020, **5**, 10145–10159.
37 I. Shahzadi, M. Islam, H. Saeed, A. Shahzadi, J. Haider, A. Haider, M. Imran, H. A. Rathore, A. Ul-Hamid and W. Nabgan, *Int. J. Biol. Macromol.*, 2023, **235**, 123874.
38 I. Shahzadi, M. Islam, H. Saeed, A. Haider, A. Shahzadi, J. Haider, N. Ahmed, A. Ul-Hamid, W. Nabgan and M. Ikram, *Int. J. Biol. Macromol.*, 2022, **220**, 1277–1286.
39 P. K. Soni, A. Bhatnagar and M. A. Shaz, *Int. J. Hydrogen Energy*, 2023, **48**, 17970–17982.
40 M. Ikram, A. Shahzadi, M. Bilal, A. Haider, A. Ul-Hamid, W. Nabgan, J. Haider, S. Ali and M. Imran, *Front. Chem.*, 2023, **11**, 1167701.
41 S. Narzary, K. Alamelu, V. Raja and B. J. Ali, *J. Environ. Chem. Eng.*, 2020, **8**, 104373.
42 Y. Astuti, A. Fauziyah, S. Nurhayati, A. Wulansari, R. Andianingrum, A. Hakim and G. Bhaduri, *Mater. Sci. Eng.*, 2016, **107**, 012006.
43 J. Yang, T. Xie, C. Liu and L. Xu, *Materials*, 2018, **11**, 1359.
44 N. Nurmalasari, Y. Yulizar and D. Apriandanu, *Mater. Sci. Eng.*, 2020, **763**, 012036.
45 Y. Wang, Y. Wen, H. Ding and Y. Shan, *J. Mater. Sci.*, 2010, **45**, 1385–1392.
46 T. Xian, X. Sun, L. Di, Y. Zhou, J. Ma, H. Li and H. Yang, *Catalysts*, 2019, **9**, 1031.
47 Z. Khazaee, A. Mahjoub, A. H. Cheshme Khavar, V. Srivastava and M. Sillanpää, *Environ. Sci. Pollut. Res.*, 2021, **28**, 50747–50766.
48 N. Motakef Kazemi and M. Yaqoubi, *Iran. J. Pharm. Res.*, 2020, **19**, 70–79.
49 H. M. Zubair Arshad, M. Imran, A. Haider, I. Shahzadi, M. Mustajab, A. Ul-Hamid, W. Nabgan, F. Medina, S. Aslam and M. Ikram, *Front. Environ. Sci.*, 2023, **11**, 528.
50 S. Condurache-Bota, C. Constantinescu, M. Praisler and N. Tigau, *Sensors*, 2015, **1**, 7–9.

51 M. Ikram, M. Saeed, J. Haider, A. Haider, A. Ul-Hamid, A. Shahzadi, W. Nabgan, A. Rafique, S. Dilpazir and S. Ali, *Appl. Nanosci.*, 2022, **12**, 2657–2670.
52 T. Chen, Q. Hao, W. Yang, C. Xie, D. Chen, C. Ma, W. Yao and Y. Zhu, *Appl. Catal., B*, 2018, **237**, 442–448.
53 P. Hao, Z. Zhao, J. Tian, Y. Sang, G. Yu, H. Liu, S. Chen and W. Zhou, *Acta Mater.*, 2014, **62**, 258–266.
54 S. P. Adhikari, H. Dean, Z. D. Hood, R. Peng, K. L. More, I. Ivanov, Z. Wu and A. Lachgar, *RSC Adv.*, 2015, **5**, 91094–91102.
55 S. S. Lee, H. Bai, Z. Liu and D. D. Sun, *Water Res.*, 2013, **47**, 4059–4073.
56 S. Lu, T. Wu, Y. Liu, H. Luo, F. Jiang, X. Nie and H. Chen, *J. Alloys Compd.*, 2022, **911**, 164980.
57 S. Munusamy, *Sustainable Chem. Processes*, 2013, **1**, 1–8.
58 W. Zhao, Y. Wang, Y. Yang, J. Tang and Y. Yang, *Appl. Catal., B*, 2012, **115**, 90–99.
59 D. Kumar, D. Banerjee, S. Sarkar, N. S. Das and K. K. Chattopadhyay, *Mater. Chem. Phys.*, 2016, **175**, 22–32.
60 S. Borthakur and L. Saikia, *J. Environ. Chem. Eng.*, 2019, **7**, 103035.
61 W. Yuan, C. Zhang, H. Wei, Q. Wang and K. Li, *RSC Adv.*, 2017, **7**, 22825–22835.
62 X. Ma, H. Yuan, Q. Qiao, S. Zhang and H. Tao, *Colloids Surf., A*, 2023, **664**, 131099.
63 Ayesha, M. Imran, A. Haider, I. Shahzadi, S. Moeen, A. Ul-Hamid, W. Nabgan, A. Shahzadi, T. Alshahrani and M. Ikram, *J. Environ. Chem. Eng.*, 2023, **11**, 110088.
64 M. Ikram, T. Inayat, A. Haider, A. Ul-Hamid, J. Haider, W. Nabgan, A. Saeed, A. Shahbaz, S. Hayat and K. Ul-Ain, *Nanoscale Res. Lett.*, 2021, **16**, 1–11.
65 T. Shujah, A. Shahzadi, A. Haider, M. Mustajab, A. M. Haider, A. Ul-Hamid, J. Haider, W. Nabgan and M. Ikram, *RSC Adv.*, 2022, **12**, 35177–35191.
66 E. Ragab, M. Shaban, A. A. Khalek and F. Mohamed, *Int. J. Biol. Macromol.*, 2021, **181**, 301–312.
67 W. J. Aziz, M. A. Abid, D. A. Kadhim and M. K. Mejbel, *Mater. Sci. Eng.*, 2020, **881**, 012099.
68 Z. Mehmood, M. Ikram, M. Imran, A. Shahzadi, A. Haider, A. Ul-Hamid, W. Nabgan, J. Haider and S. Hayat, *Process Biochem.*, 2022, **121**, 635–646.
69 S. McAuley, A. Huynh, A. Howells, C. Walpole, A. Maxwell and J. R. Nodwell, *Cell Chem. Biol.*, 2019, **26**, 1274–1282.